An assessment of thin cloud detection by applying bidirectional reflectance distribution function model-based background surface reflectance using Geostationary Ocean Color Imager (GOCI): A case study for South Korea

Hye-Won Kim, Jong-Min Yeom, Daegeun Shin, Sungwon Choi, Kyung-Soo Han, Jean-Louis Roujean

AGU PUBLICATIONS

JGR

Journal of Geophysical Research: Atmospheres

RESEARCH ARTICLE
10.1002/2017JD026707

Key Points:
- Thin cloud detection algorithm over land area was suggested with geostationary ocean color satellite imagery
- Background reflectance of the surface underneath the cloud is simulated with bidirectional reflectance distribution function model
- Agreement between CALIPSO and new cloud detection algorithm was over 94% when detecting thin cloud (altostratus and cirrus) during study period

Correspondence to:
J.-M. Yeom,
yeomjm@kari.re.kr

Citation:
Kim, H.-W., J.-M. Yeom, D. Shin, S. Choi, K.-S. Han, and J.-L. Roujean (2017), An assessment of thin cloud detection by applying bidirectional reflectance distribution function model-based background surface reflectance using Geostationary Ocean Color Imager (GOCI): A case study for South Korea, *J. Geophys. Res. Atmos.*, *122*, 8153–8172, doi:10.1002/2017JD026707.

Received 27 FEB 2017
Accepted 5 JUL 2017
Accepted article online 8 JUL 2017
Published online 10 AUG 2017

An assessment of thin cloud detection by applying bidirectional reflectance distribution function model-based background surface reflectance using Geostationary Ocean Color Imager (GOCI): A case study for South Korea

Hye-Won Kim[1], Jong-Min Yeom[1], Daegeun Shin[2], Sungwon Choi[3], Kyung-Soo Han[3], and Jean-Louis Roujean[4]

[1]Korea Aerospace Research Institute, Daejeon, South Korea, [2]Department of Atmospheric Science, Pusan National University, Busan, South Korea, [3]Department of Spatial Information Engineering, Pukyong National University, Busan, South Korea, [4]Meteo-France, Toulouse, France

Abstract In this study, a new assessment of thin cloud detection with the application of bidirectional reflectance distribution function (BRDF) model-based background surface reflectance was undertaken by interpreting surface spectra characterized using the Geostationary Ocean Color Imager (GOCI) over a land surface area. Unlike cloud detection over the ocean, the detection of cloud over land surfaces is difficult due to the complicated surface scattering characteristics, which vary among land surface types. Furthermore, in the case of thin clouds, in which the surface and cloud radiation are mixed, it is difficult to detect the clouds in both land and atmospheric fields. Therefore, to interpret background surface reflectance, especially underneath cloud, the semiempirical BRDF model was used to simulate surface reflectance by reflecting solar angle-dependent geostationary sensor geometry. For quantitative validation, Cloud-Aerosol Lidar and Infrared Pathfinder Satellite Observation (CALIPSO) data were used to make a comparison with the proposed cloud masking result. As a result, the new cloud masking scheme resulted in a high probability of detection (POD = 0.82) compared with the Moderate Resolution Imaging Spectroradiometer (MODIS) (POD = 0.808) for all cloud cases. In particular, the agreement between the CALIPSO cloud product and new GOCI cloud mask was over 94% when detecting thin cloud (e.g., altostratus and cirrus) from January 2014 to June 2015. This result is relatively high in comparison with the result from the MODIS Collection 6 cloud mask product (MYD35).

1. Introduction

Clouds are one of the first difficulties encountered when studying land surfaces or atmospheric characteristics using optical satellites. In terrestrial applications, clouds should be carefully removed to secure the inherent spectral characteristics of a surface. In atmospheric fields, such as cloud physics and precipitation, the reflected surface spectral characteristics are considered to be errors because they affect estimates of the amount of inherent cloud radiation. In particular, it is difficult to distinguish thin clouds with surface and cloud radiance, without analyzing their respective characteristics. When the radiant information of the surface and the cloud is distinguished as thick cloud, there are few difficulties. However, in the case of thin clouds, in which the surface and cloud radiation are mixed, it is difficult to detect thin clouds in both land and atmospheric fields.

Clouds generally have higher reflectivity and lower temperature than other natural bodies [*Ackerman et al.*, 1998; *Engel-Cox et al.*, 2004]. Due to the discrepancies in emissivity and temperature, thermal infrared observations indicate significant spectral contrasts between clouds and the underlying surfaces [*Liu and Liu*, 2013]. Some previous studies have proposed taking advantage of shortwave infrared (SWIR) bands to detect cirrus clouds by comparison with near-infrared (NIR) reflectance [*Gao and Kaufman*, 1995; *Wang and Shi*, 2006]. Therefore, cloud masking methods with an optical satellite are generally categorized as using either visible or IR channels [e.g., *Di Vittorio and Emery*, 2002; *Lyapustin et al.*, 2008]. *Rossow and Garder* [1993] used these two major components of visible and IR radiance to develop cloud detection schemes using International Satellite Cloud Climatology Project satellite observations. The cloud detection method of the advanced

very high resolution radiometer is composed of two visible and three IR bands [*Saunders and Kriebel*, 1988; *Gesell*, 1989]. The cloud masks for the Moderate Resolution Imaging Spectroradiometer (MODIS) are generated with 22 of 36 spectral bands of MODIS [*Ackerman et al*., 1998]. As previous studies have mentioned, simple visible and IR threshold methods offer considerable skill in cloud detection [*Ackerman et al*., 1998]. Nevertheless, when using conventional methods, it is still difficult to detect thin cloud with an optical sensor.

In this study, we conducted an assessment of thin cloud detection by interpreting surface spectral characteristics using the Geostationary Ocean Color Imager (GOCI). We used the GOCI satellite, which is mainly used for ocean observation, in the process of cloud removal for land applications, and obtained a result that was more useful for thin cloud detection than the conventional method. Previous studies have confirmed that GOCI or ocean color satellites have the potential to be utilized for land surface observations [*Nordkvist et al*., 2009; *von Hoyningen-Huene et al*., 2011; *Yeom and Kim*, 2013]. However, there is no reliable cloud mask satellite product that can be used for thin cloud, with limited GOCI or ocean color channel specification. One of the main obstacles in cloud masking with an ocean color sensor is the absence of IR channels.

GOCI, which is the one of three major payloads of the Communication, Ocean, and Meteorological Satellite (COMS), was launched by the Ariane 5 launcher at the Guiana Space Center in Kourou, French Guiana, on 27 June 2010. The main purpose of the GOCI sensor is to observe oceanic phenomena surrounding the Korean Peninsula. There are two points that should be considered for cloud removal over land surfaces using ocean color satellites. First, unlike ocean color observation satellites, such as the Coastal Zone Color Scanner, Sea-viewing Wide Field-of-view Sensor (SeaWiFS), MODIS, and Medium Resolution Imaging Spectrometer, the geostationary GOCI satellite has different observational characteristics from polar orbiting satellites. Polar orbiting satellites, using a solar-synchronous orbit, have a constant Sun angle during certain periods, especially in midlatitude regions. This means that the degree of change of surface reflectance due to the bidirectional reflectance distribution function (BRDF) effect caused by the solar angle is minimized; thus, the variation of surface reflectance by relative Sun position would be lower than that for a geostationary satellite. The effect of the Sun remains to some degree, based on the satellite viewing angle that exists within the field of view. While GOCI provides images with high temporal resolution, it has the disadvantage of having a high sensitivity to the solar angle, i.e., solar angle-dependent reflectance. Also, similar to the SeaWiFS ocean color satellite, the GOCI sensor is not equipped with IR channels. These problems will eventually affect cloud removal, which is most important for land surface assessments with optical satellites. For cloud removal, it is difficult to take into account both the absence of the IR channels of the existing ocean color satellites and also the sensitivity of the surface reflectivity to the Sun's angle, which appears in complex surface characteristics. As a result, cloud masking with a geostationary ocean color imager is not easy with conventional cloud masking methods; therefore, a new approach is needed.

In this study, an assessment of a new cloud masking method over the Korean Peninsula, with an emphasis on the land surface, was undertaken using GOCI reflectance data. The new method had the advantage of obtaining land cover data and also determining the cloud distribution. Furthermore, by comparing the realistic surface reflectance from the satellite with the simulated background surface reflectance based on the BRDF model, we could consider the probability of cloud detection, including thin clouds. In section 2, the characteristics of GOCI observations and BRDF modeling are introduced. In addition, the advanced cloud detection algorithm and cloud shadow detection are shown in detail. In section 3, results obtained by applying the masking method are presented for several cases. Section 4 considers how the cloud masking algorithm should be further developed. Finally, we summarize the results and present the conclusions of this study in section 5.

2. Materials and Methods

2.1. Data Sets

GOCI, which is the ocean color imager of COMS, is located at an altitude of 36,000 km and has a geostationary orbit. With a spatial resolution of 500 × 500 m, GOCI can cover a 2500 × 2500 km region centered on the Korean Peninsula and monitors this region 8 times per day from 00:15 UTC to 07:45 UTC. Figure 1a shows the red-green-blue (RGB) regular image of GOCI acquired on 3 May 2014. Because GOCI has a high temporal resolution at the same position, it has the ability to investigate variations in ocean color, harmful algal blooms,

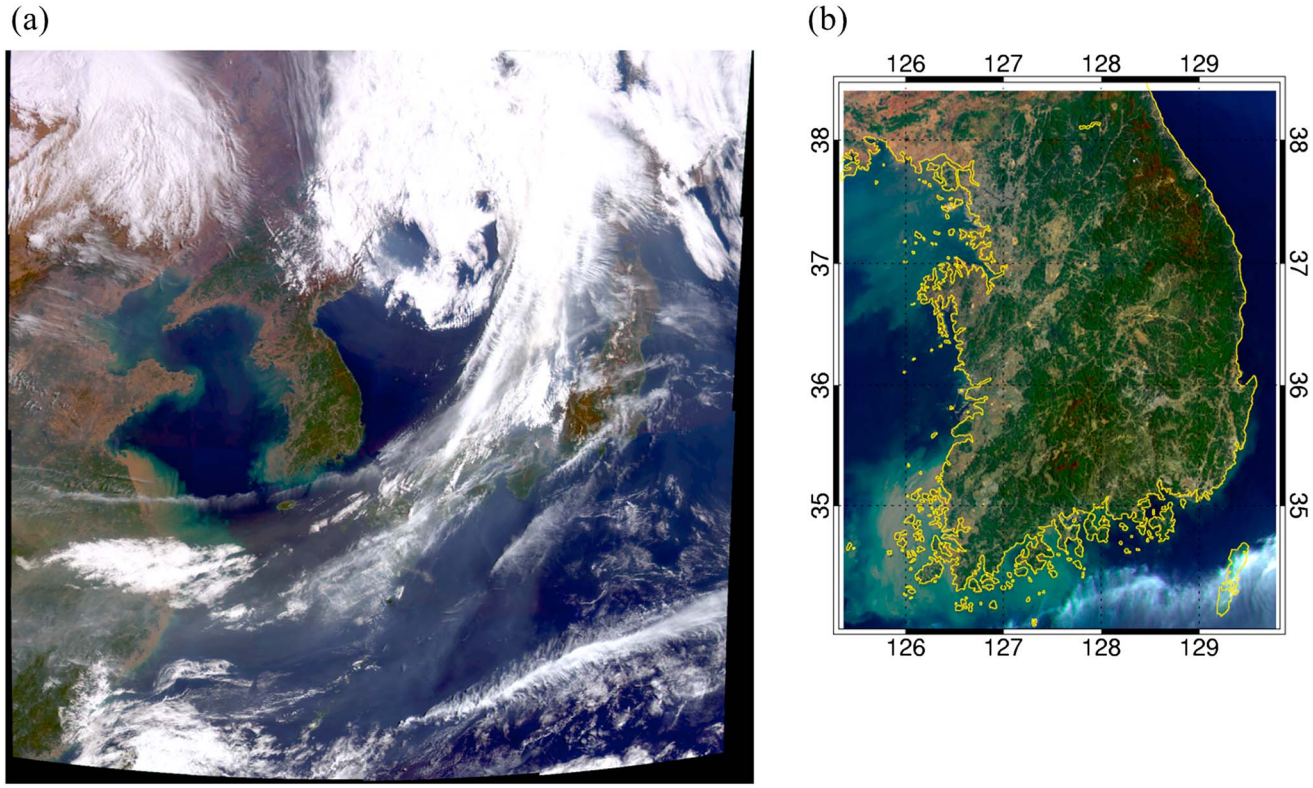

Figure 1. Geostationary Ocean Color Imager (GOCI) red-green-blue (RGB) images acquired on 3 May 2014. (a) RGB regular image and (b) cropped image of the study area.

marine ecosystem health, and the movements of suspended sediment and currents [*Faure et al*., 2008; *Ryu et al*., 2012]. The spectral channels of GOCI comprise eight different channels in the visible and NIR spectral range. The characteristics of each band are given in Table 1.

The study area was selected from full images by covering all of the Korean Peninsula (34.01°N to 37.05°N and 125.36°E to 129.78°E), except for the extreme northern parts (Figure 1b). Due to the computational burden of simulating the semiempirical BRDF model with the high temporal resolution of GOCI, the study area should be a limited region; thus, South Korea was considered appropriate. To estimate a single simulated background reflectance using the BRDF model, it is necessary to calculate 16 day composite satellite images, i.e., a maximum of 128 GOCI images, given that a composite period was applied to BRDF modeling to secure sufficient samples of cloud-free surface reflectances even in study areas with a rainy monsoon season. More detailed descriptions of BRDF modeling are provided in section 2.2. The focus of this study was the detection of clouds over land surfaces only. Therefore, land-sea masking was applied in all selected cases to remove the ocean within the study area.

Table 1. Detailed Characteristics of the Communication, Ocean, and Meteorological Satellite (COMS) Geostationary Ocean Color Imager (GOCI) Sensor

Satellite (Orbit Type)	Sensor	Band	Wavelength (nm)	Type
COMS (Geo-synchronous)	GOCI	B1	402–422	Visible
		B2	433–453	
		B3	480–500	
		B4	545–565	
		B5	650–670	
		B6	675–685	
		B7	735–755	NIR
		B8	845–885	

Table 2. Detailed Characteristics of the COMS, Aqua, and Cloud-Aerosol Lidar and Infrared Pathfinder Satellite Observation (CALIPSO) Satellites

	COMS	Aqua	CALIPSO
Orbit type	Geo-synchronous	Sun-synchronous	Sun-synchronous
Sensor	GOCI	MODIS	CALIOP
Altitude	35,786 km	705 km	705 km
Local time in ascending node (LTAN)	-	Around 1:30 P.M.	Around 1:30 P.M.
Horizontal resolution	500 m	1 km	333 m at −0.5–8.2 km altitude
Variable	Cloud mask	Cloud mask from MYD35	Vertical feature mask (VFM)
Comparable imaging time	04:15 UTC	04:25–04:55 UTC	04:00–04:35 UTC

In this study, data from the Cloud-Aerosol Lidar and Infrared Pathfinder Satellite Observation (CALIPSO) were used to validate the GOCI cloud mask. CALIPSO is in a 705 km Sun-synchronous polar orbit; the satellite passes over the Korean Peninsula twice in a 24 h period, once in the day and once at night. In this study, daytime CALIPSO data were used for validation by matching with the nearest GOCI observation time, usually 04:15 UTC. There are three distinctive sensors on the CALIPSO space-based platform: Cloud-Aerosol Lidar with Orthogonal Polarization (CALIOP), a Wide Field Camera, and an Imaging Infrared Radiometer. CALIOP, which is a lidar providing high-resolution vertical profiles of clouds, was used to detect and classify the cloud properties based on nadir viewing [*Vaughan et al*., 2005, 2009]. Especially, CALIOP can detect superthin clouds within small parts of the atmosphere, whereas passive satellite instruments cannot [*Sun et al*., 2015]. To reflect the observation differences between GOCI and CALIPSO, a parallax correction, which can reduce the positional errors between two instruments, was applied to the CALIPSO data; the correction is discussed in more detail in section 2.5. The MODIS cloud product (MYD35) was used as a comparative data set to check the accuracy of our suggested thin cloud masking algorithm [*Ackerman et al*., 2015]. MODIS is one of the most widely used satellite data sets in the world. By comparing our results with the MODIS cloud mask via time- and space-coincident lidar observations, we may verify the performance of the GOCI cloud mask with that of another passive instrument. We selected Aqua MODIS because it passed the study area from 04:30 UTC to 05:00 UTC, which was close to the CALIPSO passing time. The detailed specifications of all satellites utilized in the study are given in Table 2.

2.2. Semiempirical BRDF Modeling for Simulating Background Surface Reflectance

In this study, we used the semiempirical BRDF model [*Roujean et al*., 1992] to simulate background surface reflectance in a cloudy area. In previous studies, with optical or IR sensors, the observed top of cloud physical properties, such as cloud reflectance and brightness temperature of the cloud, have been used to discriminate cloud area with satellite imagery [*Miller et al*., 2000]. Alternatively, some studies have used the minimum reflectivity technique to estimate background surface reflectance over land and turbid water [*Herman and Celarier*, 1997; *Koelemeijer et al*., 2003; *Choi et al*., 2016]. The technique assumes that if the variation of surface reflectance is insignificant within a 30 day period over a homogenous area, the lowest top-of-atmosphere (TOA) reflectance can be considered as a clear day with the lowest atmospheric effect, as the atmospheric effect by Rayleigh scattering and aerosol mostly increases the atmospheric reflectivity in the short-wavelength region, e.g., the blue band (412 nm) of GOCI. Therefore, at least one clear day of surface reflectance is produced by selecting a minimum reflectance value during a 30 day period. In the case of a polar orbiting satellite, it would be effective to use the minimum reflectivity technique to reflect background surface reflectance under a cloudy area, because the variation of surface reflectance induced by the Sun position would reach a minimum within a 30 day period due to the satellite Sun-synchronous observation mode. However, if the minimum reflectivity technique is used to determine background surface reflectance using a geostationary satellite, it would be difficult to account for the diurnal variation of reflectance by solar variation and would result in a reduced accuracy of cloud masking.

Therefore, in this study, we proposed a new cloud masking method by determining background surface reflectance under a cloudy area based on the semiempirical BRDF model [*Roujean et al*., 1992]. Before applying the semiempirical BRDF model, a look-up table (LUT)-based atmospheric correction was performed to estimate the surface reflectance of GOCI using the 6S radiative transfer model [*Vermote et al*., 1997; *Wang*, 2003; *Nunes et al*., 2008]. When simulating LUT for atmospheric correction, MODIS atmospheric products

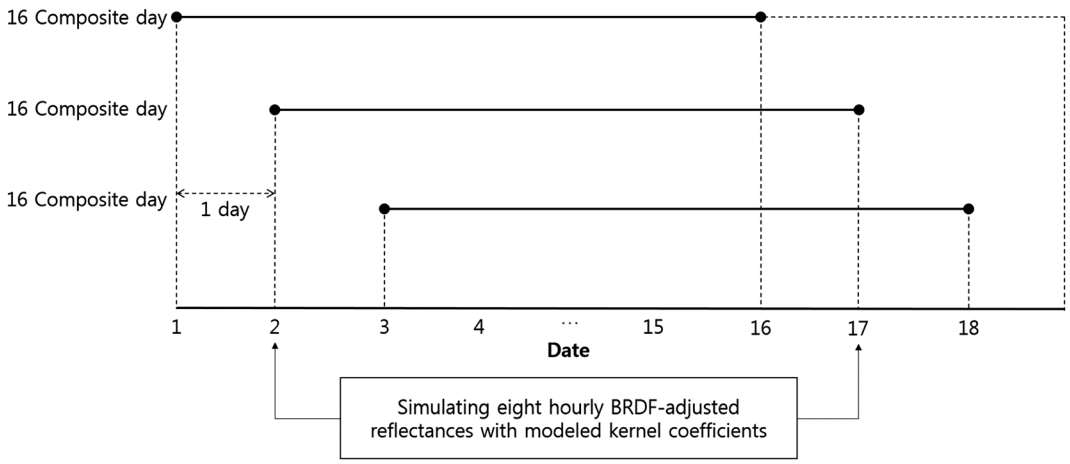

Figure 2. Concept of the composite period for bidirectional reflectance distribution function (BRDF) modeling for simulating 8-hourly BRDF-adjusted reflectance with modeled kernel coefficients.

(MOD04, MOD05, and MOD07) from NASA's Earth Observing System Data and Information System were used as input parameters to reflect atmospheric conditions such as aerosol optical depth, ozone, and water vapor. Also, if MODIS products were unavailable mainly due to cloud contamination, we substituted COMS MI atmospheric products. We adopted the semiempirical BRDF model based on Ross-thick/Li-sparse reciprocal (RTLSR) kernels to estimate the kernel coefficients and background surface reflectance [*Roujean et al.*, 1992; *Wanner et al.*, 1995; *Schaaf et al.*, 2002]. The original purpose of BRDF modeling with multitemporal satellite imagery was to simulate specific geometry reflectance, especially in the nadir direction for angular-dependent products. Using the BRDF model, the surface reflectance of specific angle geometry can be simulated with multitemporal clear-sky surface reflectance. In this study, the BRDF model was used to simulate the hourly BRDF-adjusted reflectance from 00:15 UTC to 07:45 UTC, with this time period having the same duration as the GOCI operational mode [*Lucht et al.*, 2000; *Shuai et al.*, 2008]. The semiempirical BRDF model suggested by *Roujean et al.* [1992] was expanded into a linear sum of kernels (isotropic, geometric, and volumetric) as follows:

$$\rho_{\text{measured}}(\theta_s, \theta_v, \varnothing) = f_{\text{iso}} + f_{\text{geo}} k_{\text{geo}}(\theta_s, \theta_v, \varnothing) + f_{\text{vol}} k_{\text{vol}}(\theta_s, \theta_v, \varnothing) \quad (1)$$

where θ_s and θ_v are the solar zenith and viewing zenith angles, respectively. The relative azimuth angle between solar and sensor azimuth geometry is denoted as $\varnothing$, and ρ_{measured} is the surface reflectance in a given spectral channel of GOCI. f_{geo} is the coefficient value of the Li-sparse-reciprocal geometric kernel k_{geo}, and f_{vol} is the coefficient value of the Ross-thick volumetric kernel k_{geo}. f_{iso} is the Lambertian reflectance at nadir view ($\theta_v = 0$). The BRDF model kernel coefficients were estimated independently for each gridded pixel location by inversion of equation (1), using available cloud-cleared observations for a 16 day composite period to estimate daily rolling averaged products [*Schaaf et al.*, 2002; *Lucht et al.*, 2000]. Figure 2 shows the concept of the composite period for BRDF modeling for simulating 8-hourly BRDF model-based background surface reflectance values, with modeled kernel coefficients. In this study, BRDF modeling from GOCI was estimated by periodically using a daily rolling strategy to reflect the seasonal changes of surfaces. When simulating BRDF model-based background surface reflectance (ρ_{model}) with 16 day GOCI surface reflectance, at least seven observations of cloud-free surface reflectance are required for reliable simulation results [*Schaaf et al.*, 2002; *Lucht et al.*, 2000]. For BRDF model-based background surface reflectance (ρ_{model}), the RTLSR BRDF model was used based on GOCI observation geometry, with the same θ_s , θ_v, and $\varnothing$, and using simulated BRDF model kernel coefficients.

2.3. Cloud Masking Algorithm

A cloud mask is a primary science algorithm that precedes a detailed analysis of cloud, aerosol, and land surface/ocean parameters from global observing spaceborne sensors [*Lyapustin et al.*, 2008]. However, because semitransparent clouds include two signal types, both the cloud and surface underneath, the detection of thin clouds is quite complicated [*Gao and Kaufman*, 1995; *Gao et al.*, 1998, 2002].

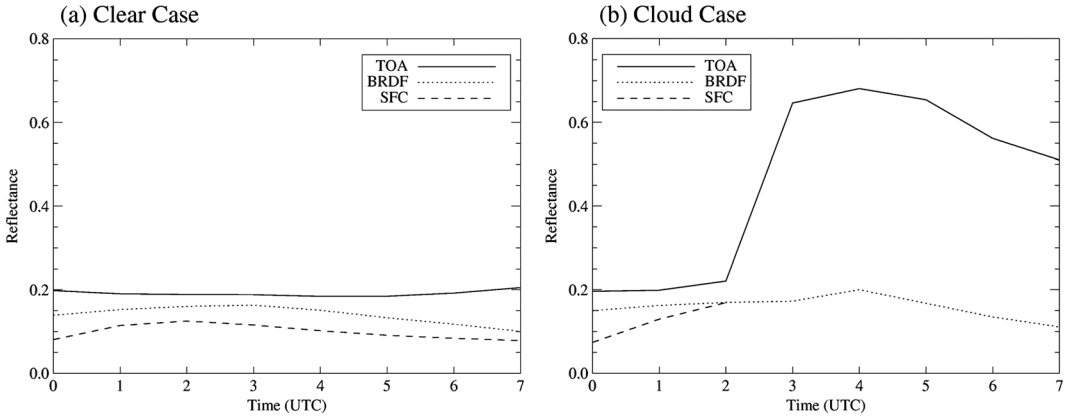

Figure 3. Examples of diurnal variation of top-of-atmosphere (TOA) reflectance, surface reflectance (SFC), and BRDF-based reflectance for (a) the clear case and (b) the cloud case.

Figure 3 shows the initial concept of the suggested cloud masking algorithm by showing examples of the diurnal variation of TOA reflectance (solid line), surface reflectance (dashed line), and BRDF model-based background surface reflectance (dotted line) from band 1 (402–422 nm) of GOCI for the clear case (Figure 3a) and the cloud case (Figure 3b). The *x* axis of the plots is UTC time; reflectance is plotted on the *y* axis. In Figure 3a for clear-sky conditions, the diurnal variations of each reflectance are well represented, indicating that it is difficult to estimate the diurnal variation of geostationary satellite reflectance using the minimum reflectivity determined for 30 days.

In Figure 3b, for the cloud case, TOA reflectance after 02 UTC increases until 04 UTC, with relatively high reflectance until the end of the day. We noticed that cloud started to approach the target area at 02 UTC, and cloud cover peaked at 04 UTC. Generally, in the case of a simple threshold method, it is easy to classify thick cloud using only the threshold of TOA reflectance without having to infer under cloud reflectance, because not only does thick cloud have a relatively higher reflectance than any other natural target but it also blocks radiance reflected by the surface. This means that a satellite sensor would detect only the spectral radiance reflected from a cloud, and not mixed values. However, the approaching cloud from 02 UTC to 03 UTC in Figure 3b would be classified as thin cloud due to its relatively smaller cloud intensity. A mixed reflectance, including that from both clouds and the surface underneath, would be expected due to transparent cloud. Therefore, unlike with the thick cloud detection algorithm, the accuracy of thin cloud detection can be determined by how accurately the surface reflectance can be estimated from the total TOA reflectance, within a mixture of the surface and cloud reflectance. In this study, we used a semiempirical BRDF model to simulate the under cloud surface reflectance for thin cloud detection as shown by the dotted line in Figure 3b.

Figure 4 shows a flowchart of the cloud masking procedure with GOCI imagery. There are three steps for thick cloud, thin cloud, and shadow detection, respectively. The first step was mainly based on conventional simple reflectance and the ratio thresholds of TOA reflectance. As shown on the left in Figure 4, a total of four channels were used to perform the first step of cloud masking. The existence of cloud was checked using the reflectance thresholds for each channel; cloudiness was detected according to the ratio between channels 6 and 8. If the pixel was not determined to be a "thick cloud" pixel in this step, the procedure advanced to step 2 processing.

Step 2 is the new method proposed in this study. This method uses the difference in reflectance between TOA and under cloud reflectance to detect the remaining cloud pixels that were not classified as thick cloud, using the reflectance threshold method used in step 1. The method has the ability to determine "thin cloud" pixels. First, we selected clear-sky areas which were referred to as "certainly clear" to determine the magnitude of the atmospheric effect between the surface and TOA. These certainly clear pixels are a necessary baseline to separate the surface underneath cloud from mixed thin cloud reflectance. The certainly clear pixels were determined from normalized difference vegetation index (NDVI) values among nonthick cloud areas, including areas of potential thin cloud. The NDVI values were obtained using visible and NIR radiation from band 5 (650–670 nm) and band 8 (845–885 nm) of GOCI, respectively. Land surface area with an NDVI

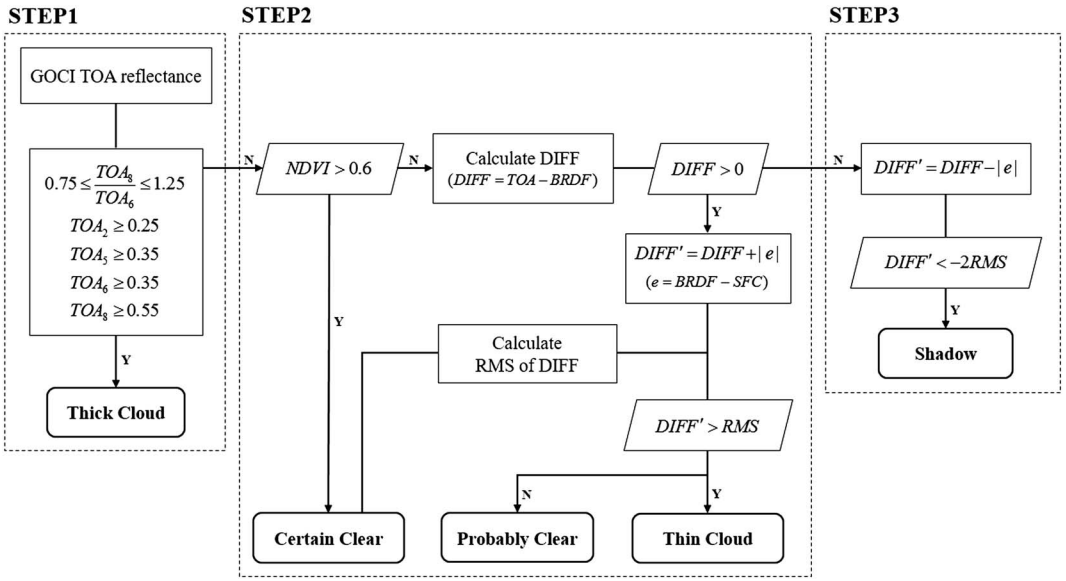

Figure 4. Schematic diagram of the cloud masking algorithm using GOCI data.

value of more than 0.6, i.e., high NDVI in *Lyapustin et al.* [2008], could be used as a clear-sky area. The NDVI threshold was empirically determined to establish the definite noncloud pixels. If we used a lower threshold, nonland pixels (e.g., cirrus or cloud shadow pixels) had the potential be included in the certainly clear category [*Simpson and Stitt*, 1998].

The RMS was calculated for all certainly clear pixels to determine the contribution of the atmospheric effect without cloud contamination. The RMS equation is as follows:

$$\mathrm{DIFF} = (\mathrm{TOA} - \mathrm{BRDF}), \tag{2}$$

$$\mathrm{RMS} = \sqrt{\frac{1}{n}\sum_{i=1}^{n} \mathrm{DIFF}_i{}^2}, \tag{3}$$

where DIFF is the difference between observed band 1 TOA reflectance and BRDF model-based surface reflectance and n is the total number of certainly clear pixels. The RMS value was used as the criteria to determine thin cloud or areas that were probably clear because we considered the RMS value to represent the contribution of atmospheric effects without contamination from clouds at the corresponding time.

For cases where the NDVI was less than 0.6 and nonthick cloud was present, the DIFF was also calculated for all undefined pixels to detect thin cloud. If the DIFF value was positive, the procedure to detect thin cloud continued; however, if the DIFF value was negative, then step 3 was performed. When the algorithm proceeded through step 2, pixels with a negative DIFF were considered to be "probably clear." A detailed description of the shadow detection process (step 3) is given in section 2.4. The BRDF model can simulate surface reflectance within the limited Sun and satellite angular range with reasonable accuracy by securing at least seven clear-sky pixels [*Han et al.*, 2004], but it still has some level of uncertainty. Therefore, we calculated DIFF′ to reflect the amount of BRDF modeling error (e), which can be estimated by subtracting atmospherically corrected surface reflectance from BRDF model-based background surface reflectance. DIFF′ represents the total atmospheric effect, including the surface underneath clouds, cloud contribution, and model uncertainty. Therefore, in this study, when compared with total TOA reflectance, a value exceeding the sum of the certainly clear atmospheric effect and BRDF model uncertainty was considered to be a cloud effect. If a difference value was larger than the RMS from certainly clear pixels, the pixel was classified as thin cloud. After processing these methods, residual pixels, which were not included in any categories (e.g., certainly clear, thick cloud, and thin cloud), were defined as probably clear pixels by default.

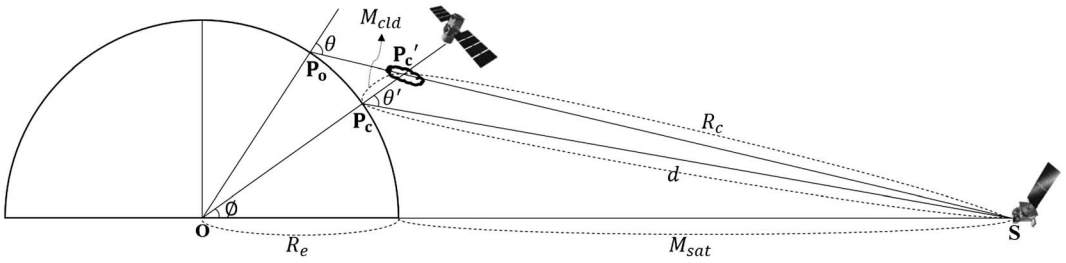

Figure 5. Schematic diagram of the parallax correction for the COMS and Cloud-Aerosol Lidar and Infrared Pathfinder Satellite Observation (CALIPSO) satellites.

2.4. Cloud Shadow Masking Algorithm

Step 3 is the cloud shadow masking algorithm and is shown in Figure 4. The main procedure used in this algorithm is exactly the same as that used in thin cloud detection, but band 8 is used instead of band 1 because the diffusive radiation in the shadows is relatively smaller at longer wavelengths (i.e., NIR and SWIR bands), making the pixels in the shadowed area darker than their surroundings [*Luo et al*., 2008; *Zhu and Woodcock*, 2012]. Thus, band 8 (845–885 nm) has the longest wavelength among all of the GOCI channels and was selected for detecting the cloud shadow. Because cloud shadow pixels are usually darker than noncloud shadow pixels, the negative DIFF value for band 8 was used, whereas the positive DIFF value for band 1 was used for the thin cloud detection. The BRDF modeling error was also reflected in the cloud shadow masking process. Based on a visual inspection, we determined a threshold value that was smaller than the negative 2RMS to detect "shadow." If the DIFF$'$ values were larger than the threshold, it was considered that the pixels were not affected by shadow effects. It was confirmed that there was no influence on cloud effects in step 2. Therefore, these pixels were defined as probably clear.

2.5. Parallax Correction for GOCI and MODIS

The validation of cloud masking using GOCI is necessary to verify our cloud masking result. However, with regard to the satellite, the cloud location above the ground can be observed differently with a different satellite zenith angle. When each satellite detects the same target in the air (such as cloud), parallax errors between two satellites arise due to the different satellite locations. The input data sets used to modify the parallax error are composed of cloud altitude, satellite zenith angle, and satellite azimuth angle. For example, when the satellite zenith angle is assumed to be 70°, cloud height is 15 km, and the satellite azimuth angle is 120°, the maximum cloud position error is about 60 km due to the parallax error [*Lee et al*., 2011]. Because the CALIOP on board the CALIPSO satellite can detect a target from directly above it, the actual position of a cloud is the same as the viewing position from the satellite. In contrast, GOCI on board the COMS satellite detects a target over the Korean Peninsula from above the equator; therefore, a difference in position between the real location and satellite data is apparent. Thus, to collocate the ground footprints of clouds for both satellites, a parallax correction has to be performed [*Vicente et al*., 2002; Pešice, 2009; *Wang et al*., 2011]. Figure 5 illustrates the parallax correction between the CALIPSO and COMS satellites.

In this study, the parallax correction method was applied in reverse to the approach presented by *Lee et al*. [2011]. *Lee et al*. [2011] studied the parallax correction between the Multifunctional Transport Satellite-2 and MODIS on board the Terra satellite. They obtained θ' by being aware of the actual cloud position (Figure 5). In the present study, the parallax correction was undertaken to convert θ to θ' for GOCI because GOCI does not have information regarding the target cloud altitude. With the value of θ, the modified point of the cloud footprint above ground as viewed from CALIPSO could be acquired. The altitude of cloud M_{cld} was determined from $\mathbf{P_c}$, i.e., the point where the ground footprint for the cloud could be obtained by the CALIOP instrument. R_e denotes the radius of the Earth. Applying the cosine rule to $\triangle\mathbf{P_cOS}$ and a quadratic formula, d, the distance from point $\mathbf{P_c}$ to point **S** can be written as follows:

$$d = \sqrt{\left(R_{\mathrm{sat}} + R_e \sin\theta'\right)\left(R_{\mathrm{sat}} - R_e \sin\theta'\right)} - R_e \cos\theta', \tag{4}$$

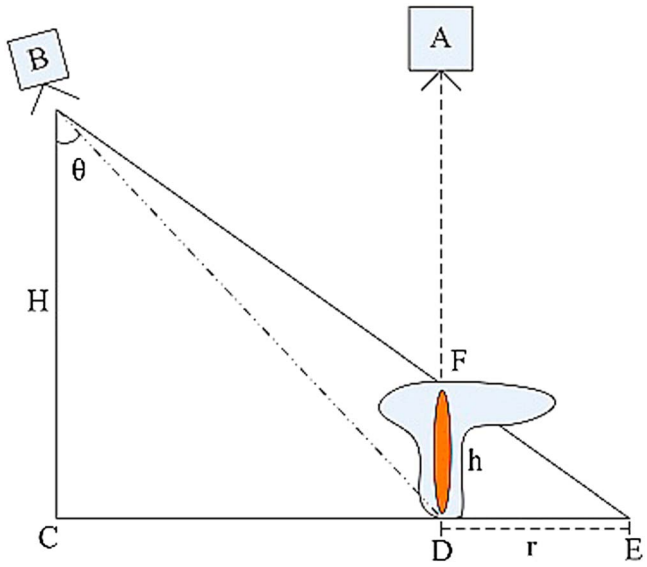

Figure 6. Schematic diagram of the parallax correction for Aqua and CALIPSO satellites (from *Wang et al.* [2011], reprinted with permission).

where R_{sat} is the distance from the center of the Earth to COMS and M_{sat} is set as 36,000 km. By applying the cosine rule to $\triangle \mathbf{P_cP_c'S}$, the distance from the cloud to COMS, R_c can be written as

$$R_c = \sqrt{{M_{cld}}^2 + d^2 - 2dM_{cld}\cos\theta'}. \quad (5)$$

By applying the sine rule to $\triangle \mathbf{P_cP_c'S}$, $\triangle \mathbf{P_cOS}$, and $\triangle \mathbf{P_c'OS}$, $\varnothing$ can be written as

$$\varnothing = \arcsin\left(\frac{d}{R_c}\sin\theta'\right) - \arcsin\left(\frac{dR_{cld}}{R_cR_{sat}}\sin\theta'\right), \quad (6)$$

where R_{cld} denotes the distance between the cloud and the center of the Earth. Applying the sine rule to $\triangle \mathbf{P_oOS}$ and $\triangle \mathbf{P_c'OS}$, we can finally obtain θ as follows:

$$\therefore \theta = \arcsin\left(\frac{R_{sat}R_{cld}}{R_eR_c}\sin\varnothing\right). \quad (7)$$

Using equations (4)–(7), the parallax correction could be applied and CALIPSO data for the point $\mathbf{P_o}$ were acquired. The corrected data for this point were used for the validation in section 3.3. Furthermore, MODIS data are used for comparisons with the results of GOCI cloud masking; the parallax correction for MODIS and CALIPSO based on *Wang et al.* [2011] was performed. The concept of this parallax correction is shown in Figure 6, which is reprinted from *Wang et al.* [2011]; a detailed description is not provided in this paper.

3. Results

3.1. Cloud Masking

One of four categories, i.e., certainly clear, probably clear, thin cloud, and thick cloud, was selected after processing the whole cloud masking algorithm by step 2. In this study, several cases with seasonal variability were selected to test the cloud masking procedure. Some significant meteorological phenomena were also included in the cases, such as the Chang-ma (one of the East Asian summer monsoons) and yellow dust from China in the spring season. The cloud mask maps and RGB images for the study area are shown in Figure 7. The meaning of each color is indicated by the color bar; detailed information of selected events is individually described in Table 3.

The thick cloud category is the output processed by step 1 consisting of the simple threshold method and the ratio method in the cloud masking algorithm. The thin cloud category is the result of the whole cloud masking algorithm used in step 2, which contains the method using the difference between TOA reflectance and BRDF model-based background surface reflectance. As a result, more cloud areas, which were not classified as cloud pixels by step 1, could be detected by step 2 of the cloud masking algorithm in all cases. Figure 7 indicates that cloud regions with a bright white color were easily detected by step 1 (deep blue). The cloud areas surrounding thick cloud regions, which were white but appeared blurred, were determined to be thin cloud by step 2 (light blue). In spring, as shown in Figure 7a, bright and thick clouds were present in the northwest region of South Korea and could be easily detected by the conventional step 1 method due to the high cloud reflectance according to the cloud mask map in Figure 7g. However, in the case of the thin cloud located in the red circle in Figure 7a, the reflectance of the cloud was low and the transmittance was sufficiently high to show the land surface form as shown in the RGB image. Therefore, it was not detected by step 1 using the threshold and band ratio method. However, processing by step 2 revealed that it was thin cloud, with a mixture of surface and cloud reflectance, due to the high transmittance obtained using BRDF model-based background surface reflectance. The results in summer were similar to those obtained in

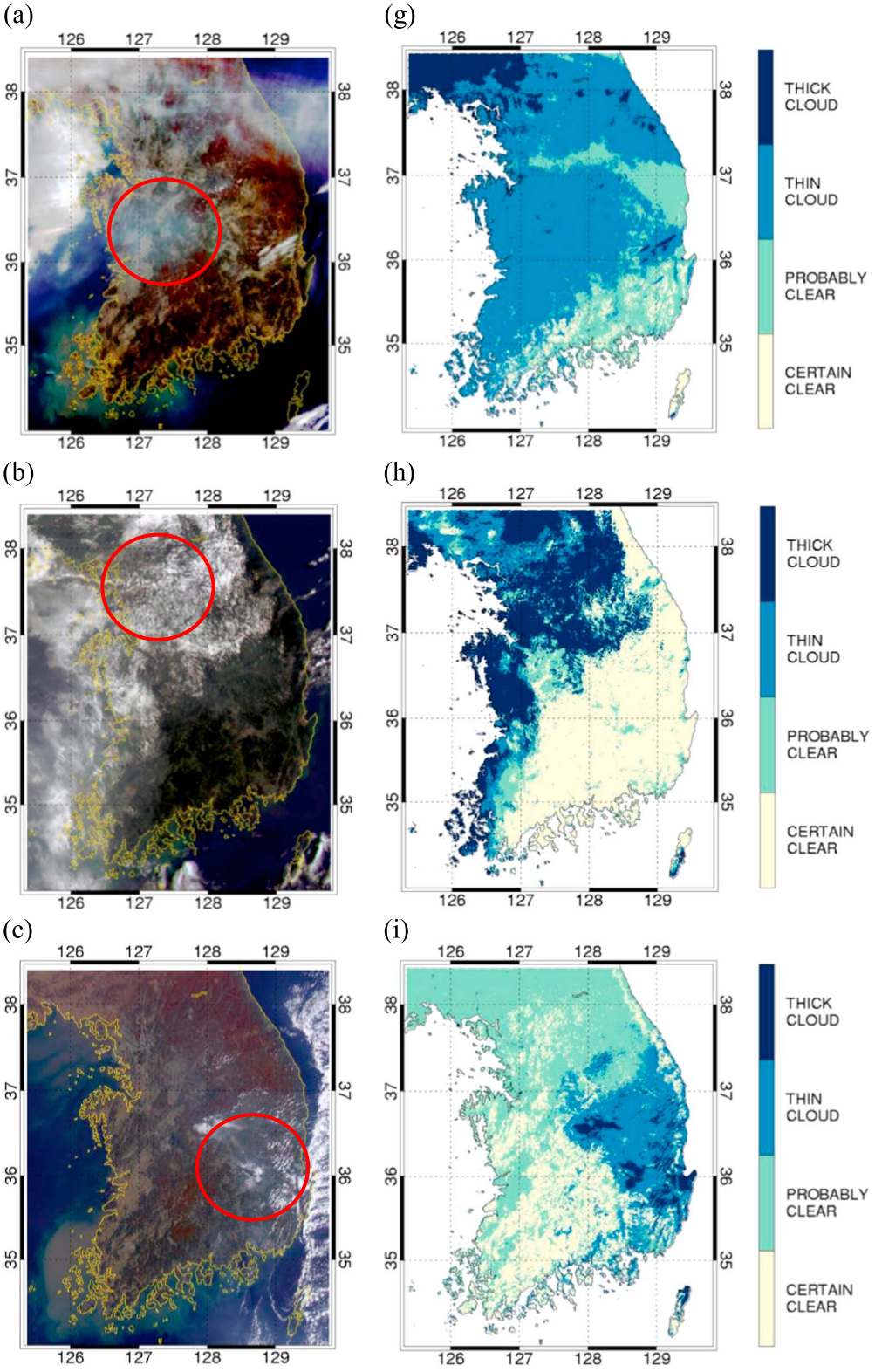

Figure 7. (a–f) RGB images and (g–l) cloud masking results for GOCI in (Figures 7a and 7g) spring (21 April 2014 00 UTC), (Figures 7b and 7h) summer (12 August 2014 00 UTC), (Figures 7c and 7i) autumn (27 October 2014 01 UTC), (Figures 7d and 7j) winter (18 December 2014 03 UTC), (Figures 7e and 7k) a yellow dust case (22 March 2015 00 UTC), and (Figures 7f and 7l) a Chang-ma case (08 August 2014 00 UTC).

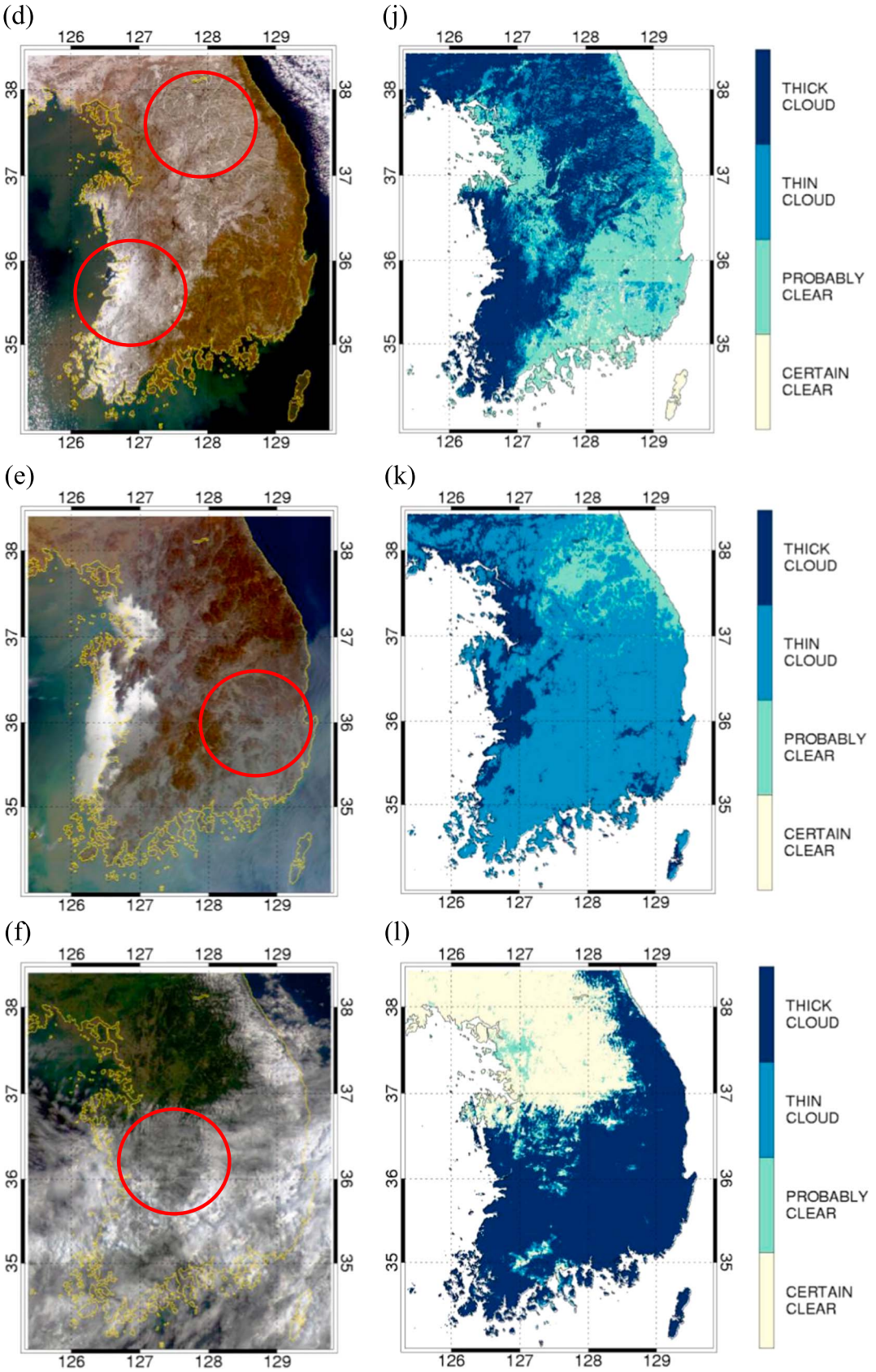

Figure 7. (continued)

Table 3. Details of Selected Cases Used to Test the Cloud Masking Procedure

List	Feature	Date	RMS	List	Feature	Date	RMS
(a)	Spring	21/04/2014 00 UTC	0.11056	(d)	Winter	18/12/2014 03 UTC	0.14676
(b)	Summer	12/08/2014 00 UTC	0.12426	(e)	Chang-ma	08/08/2014 00 UTC	0.12905
(c)	Autumn	27/10/2014 01 UTC	0.12425	(f)	Yellow dust	22/03/2015 00 UTC	0.11508

spring. In the red circular area depicted in the cloud mask map in Figure 7b, thick clouds (dark blue) were detected, but thin clouds (light blue) located between the thick clouds were difficult to detect and easy to misrepresent as land pixels in step 1. However, it can be seen that step 2 also detected thin clouds despite the high transmittance. As can be seen in the red circle in Figure 7c, clouds with high reflectance in autumn were detected in step 1, but thin clouds were also detected after applying the step 2 process.

When using the cloud detection algorithm in the winter it is difficult to discriminate snow pixels from other brightly colored pixels, such as cloud pixels [*Lyapustin et al*., 2008]. In the red circle of Figure 7d, it can be seen that thin cloud pixels, located in the eastern part of the Korean Peninsula, are not actually thin clouds. Through a visual inspection with the RGB image, the area can be assumed to be covered with snow particles or melting snow. This is problematic because the reflectance from the snow-covered surface has a combination of characteristics similar to those of thin cloud. In a previous study, the reflectance at 3.7 μm was used to distinguish snow/ice pixels from cloud pixels during the day [*Saunders and Kriebel*, 1988; *Hall et al*., 1995]. Therefore, some uncertainties in cloud masking cannot be avoided in winter because spectral wavelengths higher than the NIR channel cannot be adapted to the cloud masking algorithm used in this study.

3.2. Cloud Shadow Masking

Cloud shadow is considered to be a critical error factor in land surface applications using optical satellite data due to its abnormal darker reflectance value compared with natural surface properties. If there were no cloud shadow pixels in the scene, no shadow pixels were indicated in the cloud shadow masking map used in this study. However, there was some ambiguity in defining which category to place dark, but nonshadow surface pixels. Therefore, the criterion of a negative 2RMS was used to discriminate only definite cloud shadow pixels in the cloud masking algorithm based on step 3.

The process of cloud shadow masking is similar to that of cloud masking, as shown in Figure 4 in section 2.3. The only difference was that a shadow category was added to the cloud masking algorithm and band 8 was used for cloud shadow detection, whereas the cloud detection used band 1. Figure 8 shows the results of cloud shadow masking. To easily comprehend the result, the thin cloud and thick cloud categories were merged into one "cloud" category (Figures 8d–8f), which was represented in light blue. Through RGB images, it was recognized that cloud shadow areas were darker than other regions, even the actual surface, and the shadows were positioned on the opposite side of the Sun relative to the cloud location. In the red circle of the RGB image shown in Figure 8d, a dark cloud shadow can be seen on the left side of the cloud and its cloud shadow mask map is well matched. Figures 8b and 8c show more clearly that cloud shadows exist on the left side of clouds running both north and south. The two previous cases (Figures 8a and 8b) are images observed on 30 April and 2 May 2014 at 9 A.M. local time, and indicate that the cloud shadow was located on the west side of the cloud because the Sun was positioned to the east in the morning. The surface reflectance is dark due to the shadow effect. The final figure is an image observed in autumn on 16 October 2014. The cloud shadow located in the red circle in Figure 8c was classified using the cloud shadow detection algorithm presented in this study. In all three cases, the images were taken at 9 A.M.; however, because the final image was taken in autumn, the average solar azimuth angle was 120°, whereas in the previous spring cases it was 103°. Therefore, the position of the shadow shifted to the northwest of the cloud because the solar position was further to the south than in the spring cases. To determine the location of cloud shadows more accurately, it is necessary to know the elevation of the cloud; however, this is difficult to calculate with a GOCI image. The position of the cloud shadow can be determined to some extent by visual inspection.

3.3. Validation

We used CALIPSO satellite products as a reference due to their accuracy in detecting, monitoring, and interpreting cloud properties with a lidar observation system [*Winker et al*., 2003; *Winker et al*., 2007]. To validate the results of the cloud masking algorithm presented in this study using CALIPSO or MODIS data, a spatially

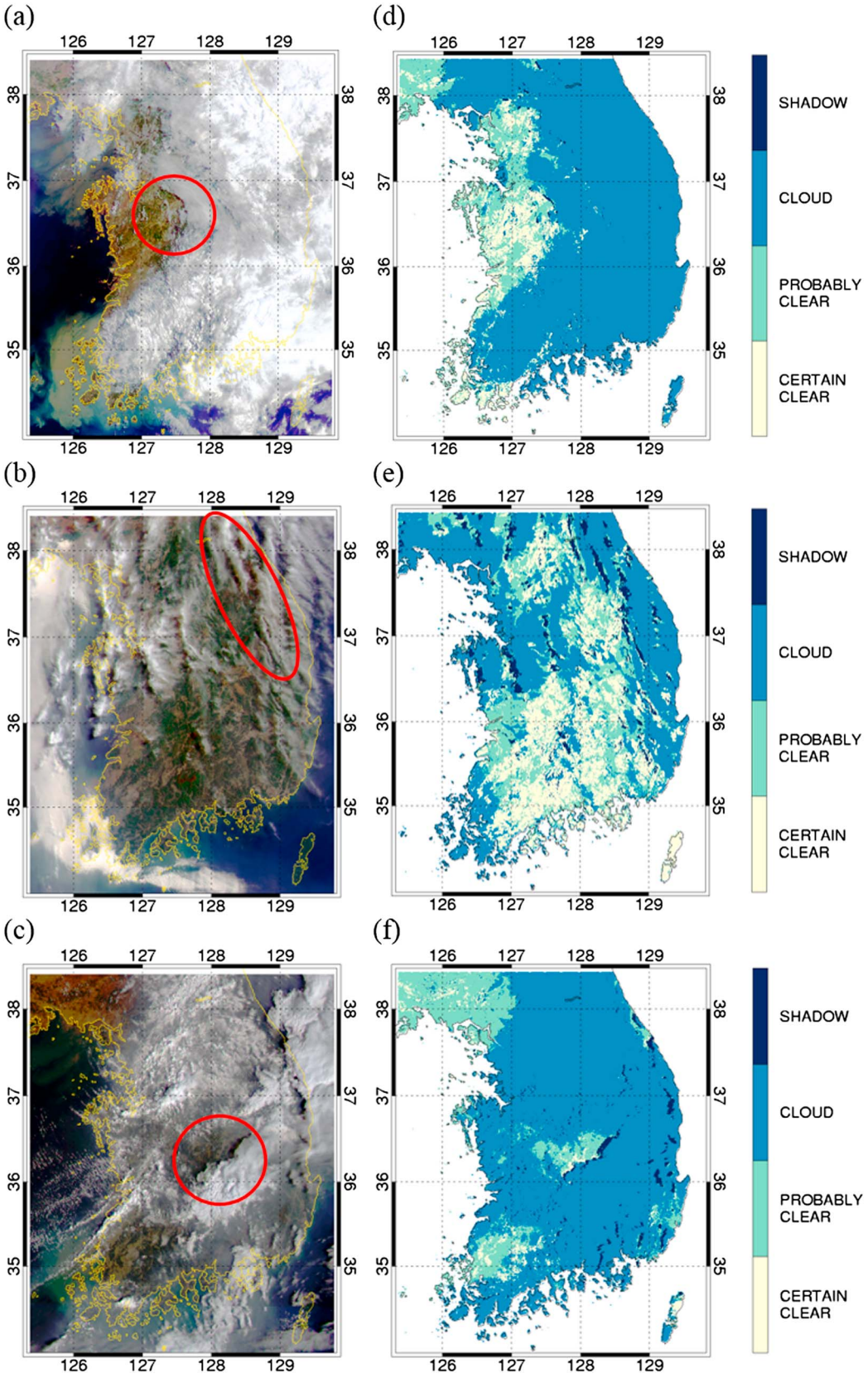

Figure 8. (a–c) RGB images and (d–f) cloud shadow masking results for GOCI in (Figures 8a and 8d) 30 April 2014 00 UTC, (Figures 8b and 8e) 02 May 2014 00 UTC, and (Figures 8c and 8f) 16 October 2014 00 UTC.

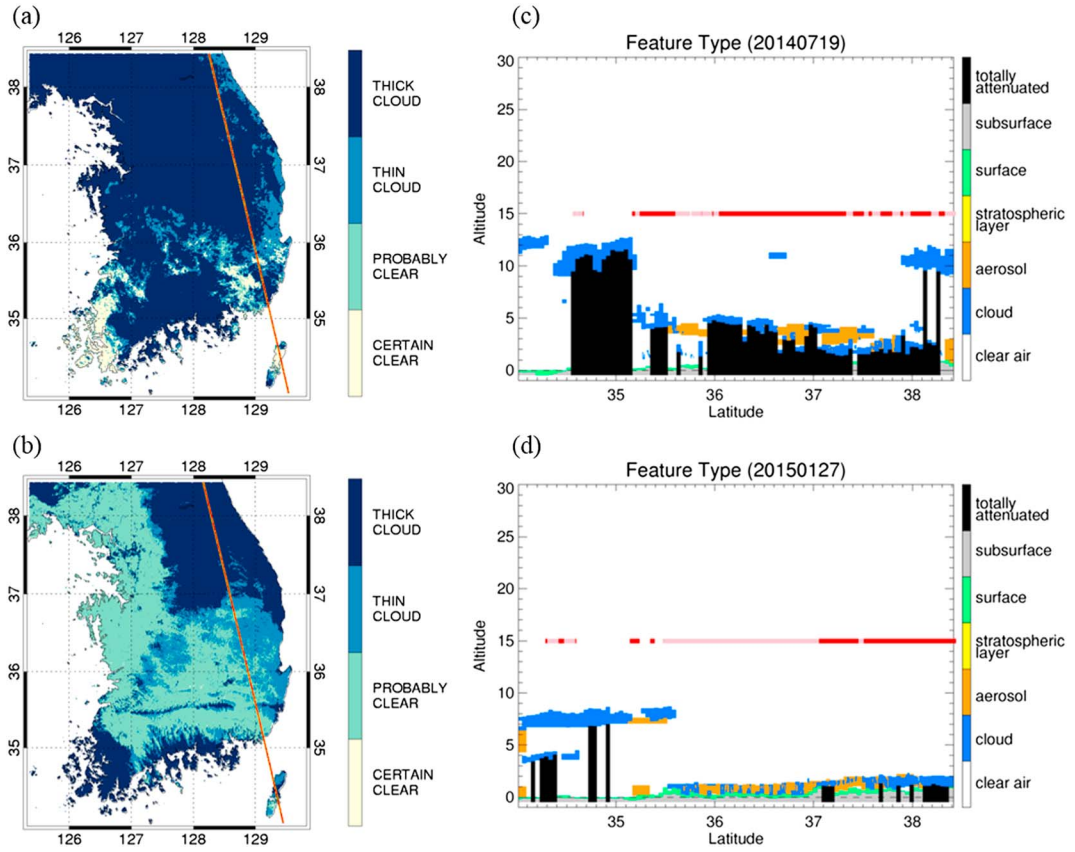

Figure 9. (a and b) CALIPSO satellite trajectory (red line) on a GOCI cloud mask map and (c and d) the vertical profile for CALIPSO vertical feature mask (VFM) on (Figures 9a and 9c) 19 July 2014 and (Figures 9b and 9d) 27 January 2015.

and temporally collocated matchup data set was used to improve the validation result. Unfortunately, two satellites with distinct observation characteristics cannot pass through the same orbit simultaneously, and the validation of the cloud detection is generally problematic [*Rossow and Garder*, 1993]. A parallax correction was applied to reduce the errors generated in images between two satellites, and the accuracy of cloud detections in this study was relatively high. Therefore, based on section 2.5, we performed parallax corrections for GOCI and MODIS to spatially match up with the CALIPSO projection. A temporal matchup was also conducted by selecting the nearest observation time of a GOCI image to CALIPSO data. The time discrepancy was a maximum of 30 min in the worst case, but in this study, it was assumed that the collocated images from different satellites were observed at the same time. Figure 9 shows examples of matchup validation data sets using the classified cloud mask map from GOCI and CALIPSO. The left column of Figure 9 indicates CALIPSO trajectories (red line) on the GOCI cloud mask map, and the right column shows the vertical profile of the CALIPSO vertical feature mask (VFM). In the VFM figures, the lines in red (thick cloud) and light red (thin cloud) drawn at 15 km altitude indicate the GOCI cloud masking results, geometrically corrected through a parallax correction. In Figures 9a and 9b, only the CALIPSO trajectory region represented by the red line was compared with the GOCI cloud mask map. In Figure 9a, there are thick clouds over all of South Korea, and thin cloudy areas in the southeast of the Korean Peninsula. Compared with the VFM in Figure 9c, the thick cloud over the northern part at 36° latitude is well matched, and the thin cloud below 36° latitude also generally agrees with GOCI (light red) and CALIPSO (blue) data. In Figures 9b and 9d, the CALIPSO and GOCI cloud type and location clearly coincide. The thick clouds in the north and the thin clouds in the latitudes between 36° and 37° also coincide. For the thick clouds extending east to west at 35.5° latitude, the cloud masking results of GOCI and CALIPSO agree.

Using this validation method, we validated the results of GOCI cloud masking from 1 January 2014 to 30 June 2015 over South Korea. The MODIS cloud product (MYD35), which is a more widely used satellite data set than CALIPSO, produced similar results to the GOCI cloud validation method considering the timing of its

Table 4. Cloud Detection Model Skill for GOCI and Moderate Resolution Imaging Spectroradiometer (MODIS) Data Compared to the CALIPSO Satellite

	Experiment 1	Experiment 2	Experiment 3	Experiment 4
Sensor	GOCI	MODIS	GOCI	MODIS
Cloud type	All cloud	All cloud	Thin cloud (altostratus and cirrus)	Thin cloud (altostratus and cirrus)
POD (S1)[a]	0.797080	-	0.859001	-
POD (S1 + S2)[b]	0.819801	0.808269	0.944849	0.936828
FAR	0.099754	0.077984	-	-
MAR	0.179035	0.191731	0.055150	0.063172
Sample number	75,281	8,692	29,519	3,631

[a]Only step 1 was applied for calculating the POD.
[b]Step 1 and step 2 were applied for calculating the POD for experiments 1 and 3.

passage and regional conditions, and would therefore be another way to objectively show the GOCI cloud mask result derived from this study. The results of the validation of the cloud masking are given in Table 4. When performing the validation of GOCI data or MODIS cloud product with CALIPSO cloud information, we considered the different cloud types, i.e., all clouds (experiments 1 and 2) and thin clouds only (experiments 3 and 4). The cloud detection algorithm proposed in this study was developed for the purpose of thin cloud detection. Therefore, by considering different cloud types, it was possible to indicate how thin cloud detection was improved by their separate representation. The CALIPSO products classify various cloud types, such as overcast, stratocumulus, cumulus, altocumulus, altostratus, cirrus, and deep convective. In this study, altostratus and cirrus were considered to be thin cloud and the remainder was classified as thick cloud.

Experiments 1 and 3 involved GOCI cloud masking for detecting all cloud and thin cloud, respectively. Experiments 2 and 4 detected all cloud and thin cloud with MODIS, with the results given in Table 4. In all cloud cases for GOCI (experiment 1) and MODIS (experiment 2), the GOCI and MODIS probability of detection (POD) values were 0.82 and 0.808, respectively. The cloud detection algorithm developed in this study had a slightly higher accuracy than MODIS, which is equipped with various channels capable of cloud detection. Some previous studies have evaluated MODIS cloud detection schemes compared with observations from satellites such as CALIPSO [e.g., *Holz et al*., 2008; *Hagihara et al*., 2010]. It was found that the MODIS 1 km cloud mask and the CALIOP 1 km averaged layer product agreement was better than 85% for both cloudy and clear-sky conditions in August 2006 and February 2007 [*Holz et al*., 2008]. *Mahesh et al.* [2004] reported that MODIS on Aqua and Geoscience Laser Altimeter System observations on the Ice, Cloud, and Land Elevation Satellite agreed in 77% of all cases. The POD for MODIS was not identified due to the differences among study areas, time periods, and observations. However, a comparison with previous studies indicated that the POD values obtained for MODIS in this study were reasonable. According to the false alarm rate in GOCI (experiment 1) and MODIS (experiment 2) data, the GOCI cloud masking method produced more overestimations than MODIS compared with CALIPSO, but the difference was less than 0.02. The missing alarm rate (MAR) of the GOCI cloud mask was lower than the MODIS value. After applying step 2 to the GOCI cloud masking algorithm, the POD was improved, indicating that the method was effective for classifying thin cloud despite GOCI being equipped with solar channels only. In the case of the thin cloud masking results, GOCI (experiment 3) had a higher POD (0.945) than the MODIS (experiment 4) value (0.937), but the small difference indicated that the GOCI cloud mask, with the BRDF model-based background surface reflectance, produced reasonable results compared with most MODIS cloud products. The lowest MAR (~0.05) value was obtained for experiment 4, which implied that the cloud masking algorithm was slightly overestimated, although there were few missing cloud pixels. Therefore, the proposed cloud masking algorithm was considered to be suitable for thin cloud detection.

4. Discussion

The cloud masking algorithm of GOCI was developed over a limited study area due to the burden of simulating the semiempirical BRDF model with high temporal resolution of GOCI. The problem of developing an algorithm in such a limited area is the uncertainty related to what should be considered as an extension of the domain. In the whole algorithm shown in Figure 4, the issue that needs to be considered when extending to the GOCI full-disk image area is the certainly clear selection problem shown in step 2. We determined that

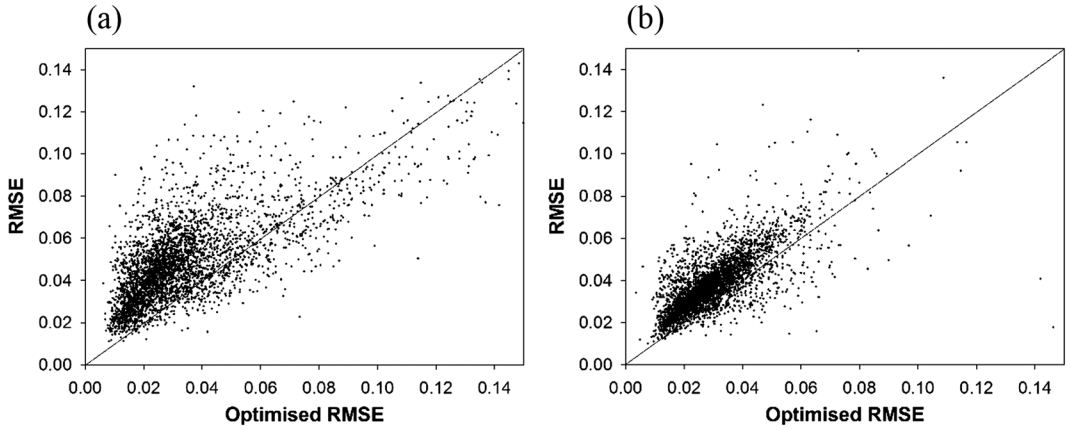

Figure 10. Scatterplot of the RMSE of the optimized BRDF modeling (*x* axis) and original BRDF (*y* axis) modeling for (a) band 1 and (b) band 8.

the certainly clear area represents clear-sky conditions when determining the magnitude of the atmospheric effect between the surface and TOA. These certainly clear pixels become a baseline for separating the surface underneath cloud from mixed thin cloud reflectance. However, it can be assumed that spatial variability is negligible for a limited area such as South Korea when a clear-sky area is selected. When GOCI is extended to a full image (2500 × 2500 km), it is difficult to ignore spatial variation. This study focused on the possibility of thin cloud detection in spectrally complicated terrestrial regions using the BRDF model-based background surface. In future work, we plan to study the clear-sky calculation and its application to an expanded research area.

When performing atmospheric correction with the 6S radiative transfer model for surface reflectance, the input parameters of the atmospheric constituents such as aerosol optical depth (AOD), water vapor, and ozone were mainly taken from the daily MODIS products (e.g., MOD04_L2, MOD05_L2, and MOD07_L2). As a geostationary satellite, GOCI makes eight measurements each day covering the whole daytime, and therefore, hourly input atmospheric parameters were required to reflect the temporal variation of gases. However, it is difficult to spatially input atmospheric products covering the whole daytime in the study area. Therefore, we assumed that the daily variation in the atmospheric constituents from the MODIS atmospheric products was negligible. Among the atmospheric constituents, AOD has more variation and makes a critical contribution to the atmospheric effects when estimating surface reflectance. Based on ground station particulate matter 2.5 data, the overall root-mean-square error (RMSE) of the AOD during the daytime was 0.123 according to *Green et al.* [2009], indicating that the expected error in the surface reflectance using the MODIS daily AOD would be less than 3% in the 6S radiative transfer model [*Yeom and Kim*, 2015]. The remaining atmospheric constituents, including water vapor and total ozone, made less contribution to the atmospheric effects.

To improve the accuracy of cloud masking with GOCI imagery, we adopted BRDF model-based background surface reflectance to reflect solar angle-dependent surface reflectance and to determine the contribution of TOA reflectance to the total surface reflectance contribution, which is also included in the thin cloud reflectance properties. However, the accuracy of the BRDF model, which uses cloud-free surface reflectance during a 16 day composite, was also reduced by unremoved thin cloud or cloud shadows. Before we performed step 2 of the cloud masking algorithm, the BRDF model-based background surface reflectance was required to determine the baseline reflectance of the surface underneath the cloud. Therefore, when simulating the BRDF model using surface reflectance in the study, we only used step 1 to mask cloud, with unremoved clouds still remaining and affecting the accuracy of the BRDF simulation. Although a sufficient number of samples were acquired from the 16 day composite and the restricted threshold values for the cloud mask algorithm would reduce the effects of removed cloud, the simulation accuracy was still affected by residual cloud. Therefore, we used the estimated cloud masking results after processing all steps in the algorithm to simulate BRDF model-based background surface reflectance again and to interpret the improvement in accuracy. The improvement in accuracy could be determined indirectly by applying the proposed cloud masking results to the land surface with GOCI.

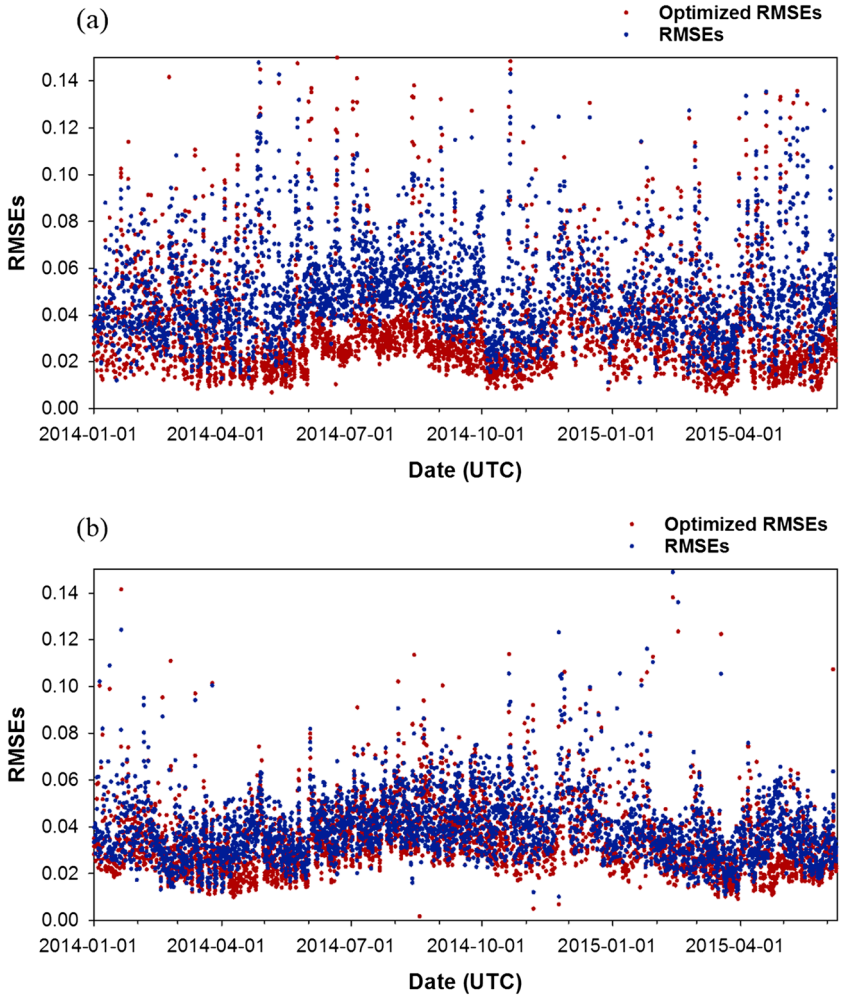

Figure 11. Seasonal variation of diurnal root-mean-square error (RMSE) for the original BRDF and optimized BRDF modeling for (a) band 1 and (b) band 8.

Figure 10 shows scatterplots for the root-mean-square errors (RMSEs) between original surface reflectance and BRDF model-based background surface reflectance, and the "optimized RMSEs" between original surface reflectance and BRDF model-based background surface reflectance using the results of the new cloud masking procedure proposed in this study. Figures 10a and 10b correspond to bands 1 and 8, respectively. The RMSE between surface reflectance (ρ_{measured}) and BRDF model-based background surface reflectance (ρ_{model}) was calculated as follows:

$$\text{RMSE} = \sqrt{\sum \frac{\left(\rho_{\text{measured}}(\theta_s, \theta_v, \varnothing) - \rho_{\text{model}}(\theta_s, \theta_v, \varnothing)\right)^2}{N}} \tag{8}$$

where N is the number of clear-sky pixels over a land surface area. The RMSEs and optimized RMSEs were calculated for every GOCI image during the study period. In Figure 10, the scatter generally follows a linear trend for both bands. The accuracy of the optimized RMSEs based on BRDF modeling, with the results of the new cloud masking procedure (also called optimized BRDF), was improved compared with the original with the optimized RMSEs mostly lower than the original values in both bands (Figures 10a and 10b). The RMSEs of the optimized BRDF were noticeably lower for band 1. This result had a positive influence on the cloud masking algorithm because band 1 is the main channel for detecting thin clouds in the new algorithm. For band 8, although the magnitude of the improvement was not as large, the optimized BRDF modeling still produced an improved result compared with the original. Figure 11 shows the temporal variation of RMSEs and optimized RMSEs. The improved performance of BRDF modeling is apparent from blue circles

representing RMSEs and red circles representing optimized RMSEs. Most RMSE values for the optimized BRDF modeling were less than the values of the original BRDF (Figures 11a and 11b). Through these plots, the seasonal variations of the RMSEs, and hence the BRDF modeling, were also apparent. In the wet summer (June-July-August) when there is a high probability of cloud cover, the temporal RMSE values for both models tended to increase. In contrast, the RMSE displayed a decreasing trend in the spring (March-April-May (MAM)) and autumn (September-October-November (SON)). Even if there were few convectional activities in winter (December-January-February), RMSE values were slightly higher than in MAM and SON. This is likely to be because snow cover in winter can be mistaken for cloud pixels. To discriminate cloud/snow cover, comparisons between visible and IR imagery are useful [*Miller et al*., 2005]. However, the detection of cloud against snow cover was limited by the narrow spectral range of GOCI.

5. Conclusions

In this study, we developed a new cloud detection algorithm optimized for thin cloud detection using BRDF model-based background surface reflectance as a key parameter to estimate the solar angle-dependent surface reflectance over the study area. Although the semiempirical BRDF model was initially developed to reduce the angular-dependent surface reflectance fluctuation induced by relative solar-target-Sun geometry, it also can be used to simulate the background surface reflectance by representing specific sensor geometry. Unlike previous cloud mask algorithms, the algorithm we proposed concentrated on possible surface effects under clouds. Thus, the background surface reflectance derived from the BRDF modeling was computed to interpret these surface effects for complex land surfaces. We focused on the cloud masking results because cloud detection was implemented without IR channels and a comparable performance to that of MODIS was achieved, indicating that the new method would be an effective alternative cloud masking method for optical satellites. To validate our result, CALIPSO products were used as a reference. The cloud detection results over the Korean Peninsula were slightly better than those of MODIS, which was used for comparison. The POD value of 0.945 indicated that this algorithm performed well in the detection of thin cloud compared with the MODIS POD of 0.937. Compared with previous studies of MODIS cloud masking results [e.g., *Mahesh et al*., 2004; *Holz et al*., 2008; *Hagihara et al*., 2010], the new method was considered to be suitable for masking thin cloud. By applying the new cloud mask data to a BRDF simulation, it was observed that the BRDF modeling performance improved. Despite the advantages mentioned above, the cloud masking algorithm was unable to detect cloud against a snow cover background due to lack of appropriate spectral channels. This problem needs to be resolved in future studies. Although the study area was limited to the Korean Peninsula in this study, it will be expanded to the whole GOCI imaging area, including Japan and the eastern part of China, in the future.

We believe that the new thin cloud masking algorithm has the potential to be used by future satellites. GOCI-II, which is the next-generation payload of GOCI, is under development by the Korea Aerospace Research Institute and is scheduled to be launched in 2019. The cloud masking algorithm we have developed would also be suitable for GOCI-II, because it has a similar spectral range as GOCI. Several ocean color satellites are also planned to be launched in the near future by NASA, including Geostationary Satellite of Coastal and Air Pollution Events and Plankton, Aerosol, Cloud, and ocean Ecosystem. In addition, the cloud masking algorithm can be adapted to not only ocean color satellites but also other Earth observations that have a short spectral range. The European Space Agency has developed Fluorescence Explorer, which acquires vegetation maps from across the world in the visible spectral range (500–880 nm) in a Sun-synchronous orbit, and will be launched in 2022. Ocean color satellites and visible spectral sensors loaded on satellites are constantly being planned for launch in the future. Therefore, we expect that our new cloud masking algorithm using the background surface reflectance can be implemented to detect clouds effectively, including thin cloud, by a range of satellites using visible spectral channels.

Acknowledgments
This research was a part of the project titled "Research for Applications of Geostationary Ocean Color Imager," funded by the Ministry of Oceans and Fisheries, Korea. This work was supported by "Development of Scene Analysis and Surface Algorithms" project, funded by ETRI, which is a subproject of "Development of Geostationary Meteorological Satellite Ground Segment (NMSC-2016-01)" program funded by NMSC (National Meteorological Satellite Center) of KMA (Korea Meteorological Administration). We thank the Korea Institute of Ocean Science and Technology for providing the GOCI data. The GOCI data can be obtained from http://kosc.kiost.ac/. MODIS data are from the NASA's Earth Observing System Data and Information System: http://reverb.echo.nasa.gov/. CALIPSO cloud products were obtained from the NASA Langley Research Center Atmospheric Science Data Center. The results of GOCI cloud masking presented in Figures 7 and 8 are available from the author upon request (yeomjm@kari.re.kr). Finally, we thank all three reviewers and the journal Editor whose comments have improved the clarity of our paper.

References

Ackerman, S. A., K. I. Strabala, W. P. Menzel, R. A. Frey, C. C. Moeller, and L. E. Gumley (1998), Discriminating clear sky from clouds with MODIS, *J. Geophys. Res.*, *103*(D24), 32,141–32,157, doi:10.1029/1998JD200032.

Ackerman, S. A., et al. (2015), *MODIS Atmosphere L2 Cloud Mask Product (35_L2)*, NASA MODIS Adaptive Processing System, Goddard Space Flight Center, USA, doi:10.5067/MODIS/MOD35_L2.006.

Choi, M. J., et al. (2016), GOCI Yonsei Aerosol Retrieval (YEAR) algorithm and validation during the DRACON-NE Asia 2012 campaign, *Atmos. Meas. Tech.*, *9*, 1377–1398.

Di Vittorio, A. V., and W. J. Emery (2002), An automated, dynamic threshold cloud-masking algorithm for daytime AVHRR images over land, *IEEE Trans. Geosci. Remote Sens.*, *40*(8), 1682–1694.
Engel-Cox, J., C. H. Holloman, B. W. Coutant, and R. M. Hoff (2004), Qualitative and quantitative evaluation of MODIS satellite sensor data for regional and urban scale air quality, *Atmos. Environ.*, *38*(16), 2495–2509.
Faure, F., P. Coste, and G. Kang (2008), The GOCI instrument on COMS mission—The first Geostationary Ocean Color Imager, in *Proceedings of the International Conference on Space Optics (ICSO)*, vol. *6*, pp. 1–6. [Available at http://www.ioccg.org/sensors/GOCI-Faure.pdf.]
Gao, B.-C., and Y. J. Kaufman (1995), Selection of the 1.375-μm MODIS channel for remote sensing of cirrus clouds and stratospheric aerosols from space, *J. Atmos. Sci.*, *52*(23), 4231–4237.
Gao, B.-C., Y. J. Kaufman, W. Han, and W. J. Wiscombe (1998), Correction of thin cirrus path radiances in the 0.4–1.0 μm spectral region using the sensitive 1.375 μm cirrus detecting channel, *J. Geophys. Res.*, *103*(D24), 32,169–32,176, doi:10.1029/98JD02006.
Gao, B.-C., Y. J. Kaufman, D. Tanre, and R. P. Li (2002), Distinguishing tropospheric aerosols from thin cirrus clouds for improved aerosol retrievals using the ratio of 1.38-μm and 1.24-μm channels, *Geophys. Res. Lett.*, *29*(18), 36-1–36-4, doi:10.1029/2002GL015475.
Gesell, G. (1989), An algorithm for snow and ice detection using AVHRR data: An extension to the APOLLO software package, *Int. J. Remote Sens.*, *10*(4–5), 897–905, doi:10.1080/01431168908903929.
Green, M., S. Kondragunta, P. Ciren, and C. Xu (2009), Comparison of GOES and MODIS aerosol optical depth (AOD) to Aerosol Robotic Network (AERONET) AOD and IMPROVE $PM_{2.5}$ mass at Bondville, Illinois, *J. Air Waste Manage. Assoc.*, *59*(9), 1082–1091.
Hagihara, Y., H. Okamoto, and R. Yoshida (2010), Development of a combined CloudSat-CALIPSO cloud mask to show global cloud distribution, *J. Geophys. Res.*, *115*, D00H33, doi:10.1029/2009JD012344.
Hall, D. K., G. A. Riggs, and V. V. Salomonson (1995), Development of methods for mapping global snow cover using Moderated Resolution Imaging Spectroradiometer data, *Remote Sens. Environ.*, *54*, 127–140.
Han, K. S., J. L. Champeaux, and J. L. Roujean (2004), A land cover classification product over France at 1 km resolution using SPOT4/VEGETATION data, *Remote Sens. Environ.*, *92*, 52–66.
Herman, J. R., and E. A. Celarier (1997), Earth surface reflectivity climatology at 340–380 nm from TOMS data, *J. Geophys. Res.*, *102*(D23), 28,003–28,011.
Holz, R. E., S. A. Ackerman, F. W. Nagle, R. Frey, S. Dutcher, R. E. Kuehn, M. A. Vaughan, and B. Baum (2008), Global Moderate Resolution Imaging Spectroradiometer (MODIS) cloud detection and height evaluation using CALIOP, *J. Geophys. Res.*, *113*, D00A19, doi:10.1029/2008JD009837.
Koelemeijer, R. B. A., J. F. De Haan, and P. Stammes (2003), A database of spectral surface reflectivity in the range 335–772 nm derived from 5.5 years of GOME observations, *J. Geophys. Res.*, *108*(D2), 4070, doi:10.1029/2002JD002429.
Lee, W. S., Y. S. Kim, D. H. Kim, and C. Y. Chung (2011), The parallax correction to improve cloud location error of geostationary meteorological satellite data, *Korean Can. J. Remote. Sens.*, *27*(2), 99–105.
Liu, R., and Y. Liu (2013), Generation of new clouds masks from MODIS land surface reflectance products, *Remote Sens. Environ.*, *133*, 21–37.
Lucht, W., C. B. Schaaf, and A. H. Strahler (2000), An algorithm for the retrieval of albedo from space using semiempirical BRDF models, *IEEE Trans. Geosci. Remote Sens.*, *38*(2), 977–998.
Luo, Y., A. P. Trishchenko, and K. V. Khlopenkov (2008), Developing clear-sky and cloud shadow mask for producing clear-sky composites at 250-meter spatial resolution for the seven MODIS land bands over Canada and North America, *Remote Sens. Environ.*, *112*, 4167–4185.
Lyapustin, A., Y. Wang, and R. Frey (2008), An automatic cloud mask algorithm based on time series of MODIS measurements, *J. Geophys. Res.*, *113*, D16207, doi:10.1029/2007JD009641.
Mahesh, A., M. A. Gray, S. P. Palm, W. D. Hart, and J. D. Spinhirne (2004), Passive and active detection of clouds: Comparisons between MODIS and GLAS observations, *Geophys. Res. Lett.*, *31*, L04108, doi:10.1029/2003GL018859.
Miller, S. D., G. L. Stephens, C. K. Drummond, A. K. Heidinger, and P. T. Partain (2000), A multisensory diagnostic satellite cloud property retrieval scheme, *J. Geophys. Res.*, *105*(D15), 19,955–19,971.
Miller, S. D., T. F. Lee, and R. L. Fennimore (2005), Satellite-based imagery techniques for daytime cloud/snow delineation from MODIS, *J. Appl. Meteorol.*, *44*(7), 987–997.
Nordkvist, K., H. Loisel, and L. D. Gaurier (2009), Cloud masking of SeaWiFS images over coastal waters using spectral variability, *Opt. Express*, *17*, 12,246–12,258.
Nunes, A. S. L., A. R. S. Marcal, and R. A. Vaughan (2008), Fast over-land atmospheric correction of visible and near-infrared satellite images, *Int. J. Remote Sens.*, *29*(12), 3523–3531.
Pešice, P. (2009), Parallax correction of Meteosat images using temperature profiles, radar echotops and combined method, *J. Surv. Eng.*, *120*(3), 115–127.
Roujean, J. L., M. Leroy, and P. Y. Deschamps (1992), A bidirectional reflectance model of the Earth's surface for the correction of remote sensing data, *J. Geophys. Res.*, *97*(D18), 20,445–20,468.
Rossow, W. B., and L. C. Garder (1993), Cloud detection using satellite measurements of infrared and visible radiances for ISCCP, *J. Clim.*, *6*(12), 2341–2369.
Ryu, J. H., H. J. Han, S. Cho, Y. J. Park, and Y. H. Ahn (2012), Overview of Geostationary Ocean Color Imager (GOCI) and GOCI Data Processing System (GDPS), *Ocean Sci. J.*, *47*(3), 223–233.
Saunders, R. W., and K. T. Kriebel (1988), An improved method for detecting clear sky and cloudy radiances from AVHRR data, *Int. J. Remote Sens.*, *9*(1), 123–150.
Schaaf, C. B., et al. (2002), First operational BRDF, albedo nadir reflectance products from MODIS, *Remote Sens. Environ.*, *83*(1), 135–148.
Shuai, Y., C. B. Schaaf, A. H. Strahler, J. Liu, and Z. Jiao (2008), Quality assessment of BRDF/albedo retrievals in MODIS operational system, *Geophys. Res. Lett.*, *35*, L05407, doi:10.1029/2007GL032568.
Simpson, J. J., and J. R. Stitt (1998), A procedure for the detection and removal of cloud shadow from AVHRR data over land, *IEEE Trans. Geosci. Remote Sens.*, *36*(3), 880–897.
Sun, W., R. R. Baize, G. Videen, Y. Hu, and Q. Fu (2015), A method to retrieve super-thin cloud optical depth over ocean background with polarized sunlight, *Atmos. Chem. Phys.*, *15*, 11,909–11,918, doi:10.5194/acp-15-11909-2015.
Vaughan, M. A., D. M. Winker, and K. A. Powell (2005), Part 2: Feature detection and layer properties algorithms. CALIOP Algorithm Theoretical Basis Document. PC-SCI-202.01, 87.
Vaughan, M. A., K. A. Powell, D. M. Winder, C. A. Hostetler, R. E. Kuehn, W. H. Hunt, B. J. Getzewich, S. A. Young, Z. Liu, and M. J. McGill (2009), Fully automated detection of cloud and aerosol layers in the CALIPSO lidar measurements, *J. Atmos. Oceanic Technol.*, *26*, 2310–2323, doi:10.1175/2009JTECHA1228.1.

Vermote, E. F., D. Tanré, J. L. Deuze, M. Herman, and J. J. Morcette (1997), Second simulation of the satellite signal in the solar spectrum, 6S: An overview, *IEEE Trans. Geosci. Remote Sens.*, *35*(3), 675–686.

Vicente, G. A., J. C. Davenport, and R. A. Scofield (2002), The role of orographic and parallax corrections on real time high resolution satellite rainfall rate distribution, *Int. J. Remote Sens.*, *23*(2), 221–230, doi:10.1080/01431160010006935.

von Hoyningen-Huene, W., J. Yoon, M. Vountas, L. G. Istomina, G. Rohen, T. Dinter, A. A. Kokhanovsky, and J. P. Burrows (2011), Retrieval of spectral aerosol optical thickness over land using ocean color sensors MERIS and SeaWiFS, *Atmos. Meas. Tech.*, *4*(2), 151–171, doi:10.5194/amt-4-151-2011.

Wang, M. (2003), An efficient method for multiple radiative transfer computations and the lookup table generation, *J. Quant. Spectrosc. Radiat. Transfer*, *78*(3), 471–480.

Wang, M., and W. Shi (2006), Cloud masking for ocean color data processing in the coastal regions, *IEEE Trans. Geosci. Remote Sens.*, *44*(11), 3196–3105, doi:10.1109/TGRS.2006.876293.

Wang, C., Z. J. Luo, and X. Huang (2011), Parallax correction in collocating CloudSat and Moderate Resolution Imaging Spectroradiometer (MODIS) observations: Method and application to convection study, *J. Geophys. Res.*, *116*, D17201, doi:10.1029/2011JD016097.

Wanner, W., X. Li, and A. H. Strahler (1995), On the derivation of kernels for kernel-driven models of bidirectional reflectance, *J. Geophys. Res.*, *100*, 21,077–21,089.

Winker, D. M., J. R. Pelon, and M. P. McCormick (2003), The CALIPSO mission: Spaceborne lidar for observation of aerosols and clouds, in *Third International Asia-Pacific Environmental Remote Sensing of the Atmosphere, Ocean, Environment, and Space*, *Int. Soc. Opt. Photon.*, vol. 4893, pp. 1–11.

Winker, D. M., W. H. Hunt, and M. J. McGill (2007), Initial performance assessment of CALIOP, *Geophys. Res. Lett.*, *34*, L19803, doi:10.1029/2007GL030135.

Yeom, J. M., and H. O. Kim (2013), Feasibility of using Geostationary Ocean Colour Imager (GOCI) data for land applications after atmospheric correction and bidirectional reflectance distribution function modelling, *Int. J. Remote Sens.*, *34*(20), 7329–7339.

Yeom, J. M., and H. O. Kim (2015), Comparison of NDVIs from GOCI and MODIS data towards improved assessment of crop temporal dynamics in the case of paddy rice, *Remote Sens.*, *7*(9), 11,326–11,343.

Zhu, Z., and C. E. Woodcock (2012), Object-based cloud and cloud shadow detection in Landsat imagery, *Remote Sens. Environ.*, *118*, 83–94.